Diadiponitrilelithium hexafluorophosphate: a soft-Solid Co-Crystalline Electrolyte Combining Advantages of Organic and Ceramic Electrolytes

Prabhat Prakash[a,b], Birane Fall[a], Jordan Aguirre[a], Parameswara Rao Chinnam[c], Sumanth Chereddy[a], Dmitriy Dikin[d], Arun Venkatnathan[b], Stephanie L. Wunder[a]*, Michael J. Zdilla[a]**

[a]Department of Chemistry, Temple University, 1901 N. 13th St., Philadelphia, PA 19086, USA

[b]Department of Chemistry and Centre for Energy Science, Indian Institute of Science Education and Research, Dr. Homi Bhabha Road, Pashan, Pune: 411008, India.

[c]Energy Storage & Advanced Transportation Department, Idaho National Laboratory, Idaho Falls, ID 83415

[d]Mechanical Engineering Department, College of Engineering, Temple University, 1947 North 12th St., Philadelphia, PA 19122.

ABSTRACT

Soft solid electrolyte materials are promising alternative choices for conventional battery electrolytes. Here, we have synthesized, characterized and calculated structural, thermal and electrochemical properties of an adiponitrile-based lithium-ion electrolyte which combines the advantages of organic and ceramic materials. This solid material is $(Adpn)_2LiPF_6$, (Adpn =

adiponitrile) wherein (Adpn)-based channels solvate Li^+ ions through weak C≡N---Li^+ contacts. The surface of the crystal is a liquid nanolayer that binds the grains so that ionically conductive pellets are easily formed without high pressure/temperature treatments, which self-heals if fractured and which provide liquid-like conduction paths through the grain boundaries. High conductivity ($\sigma \sim 10^{-4}$ S/cm) and high lithium-ion transference number ($t_{Li^+} = 0.54$) result from weak interactions between "hard" (charge-dense) Li^+ ions and "soft" (electronically polarizable) -C≡N, compared with the stronger interactions of previously reported "hard" ether oxygen contacts of polyethylene oxide (PEO) or glymes. The proposed mechanism of conduction is one in which Li^+ ion migration occurs preferentially along the low activation energy path at the co-crystal grain boundaries and within the interstitial regions between the co-crystals, with bulk conductivity comprising a smaller but extant contribution to the observed conductivity. $(Adpn)_2LiPF_6$(s) has a wide electrochemical stability window of 0 to 5 V. $Li^0/(Adpn)_2LiPF_6/LiFePO_4$ cells exhibit cycling for > 50 cycles at C/20, C/10, C/5 rates with capacities of 140 mAh-g^{-1} to 100 mAh-g^{-1} and Coulombic efficiencies ~ 99%, and mitigation of the deleterious reactions with Li metal due to the high ionic strength. LTO/$(Adpn)_2LiPF_6$/NMC622 full cells were cycled at C-rates of C/20 to 1C with Coulombic efficiencies > 96%, with no dendritic failure after 100 cycles. Novel MD approaches addressing multiple conduction pathways and PWDFT calculations offer insights into the molecular basis of the physical and conductivity properties.

INTRODUCTION

The need for replacement of volatile liquid electrolytes to improve safety in lithium-ion batteries (LIB) and to enable the use of metallic lithium in next-generation solid-state batteries has generated interest in the development of solid electrolytes. These have included polymers, polymer gels with nonvolatile liquids, and inorganic materials[1–3]. The investigation of lithium or sodium ion-conducting ceramics has yielded a wide range of oxide and sulfide-based materials[4] that are under active investigation as solid electrolytes for LIB or sodium-ion batteries (SIB). While these can have good ionic conductivities (σ) and lithium-ion transference numbers (t_{Li^+}, the fraction of charge carried by Li^+), there are still problems associated with lithium dendrite growth during recharge, and poor interfacial contact between the electrolyte and the electrodes. We have been investigating a new class of solid electrolytes: salt-organic co-crystals (also referred to as solvates) of lithium and sodium salts with weakly ligating molecular organic compounds. Similar to lithium-ion-conducting ceramics (LICC), these new "soft" co-crystals also have channels for ion migration but are not necessarily single-ion conductors. Unlike the rigid anionic lattices of ceramic electrolytes, the channels in the "soft" co-crystals consist of weakly Lewis basic donor groups of organic molecules, and in some examples, there are no Li···anion contacts[5]. Previously reported solvates of lithium salts with polyethylene oxide (PEO)[6,7] or glymes, $CH_3O\text{-}(CH_2CH_2O)_{n=1\text{-}5}\text{-}CH_3$,[8,9] can have ionic conductivities higher than their respective molten phases[7]. Nevertheless, ionic conductivities are very low ($\sigma \sim 10^{-7}$ S/cm for PEO solvates[7–10] and $\sigma \sim 10^{-6}$ S/cm for glyme solvates[9]) due to the tight chelation of the "hard" (non-polarizable) lithium ions with the "hard" ether oxygen donors. Nitriles and other triple bonded systems are known to be electronically soft due to polarizability, characterizable by the hardness factor.[11] For acetonitrile, the hardness factor is ~7.5, softer than harder ligands such as water (9.5) and ethers (8.0). Previous work in other

63 groups[12] and in our group has focused on co-crystals of lithium (or sodium) salts with a
64 coordinating ligand that has "soft" (polarizable), weakly electron-donating atoms, e.g. dimethyl
65 formamide (DMF) with LiCl[13] or $NaClO_4$[14], isoquinoline with LiCl[15], or adiponitrile (Adpn) with
66 $NaClO_4$[16], where the weaker binding promotes higher conductivity. Unlike inorganic ceramics
67 where grain boundaries can be resistive, in the case of the soft-solid cocrystals, the grain
68 boundaries are fluid, permitting easy reformation upon cracking. Some of these cocrystals melt at
69 moderate temperatures,[14,16] and can therefore be melt-cast, in contrast with inorganic electrolytes,
70 where the grains need to be sintered at high pressures and temperatures, but early examples were
71 incompatible with high voltages and electrode materials relevant to commercial batteries.

72 In the current work, soft co-crystals formed between $LiPF_6$ and Adpn are investigated
73 experimentally and theoretically. The components of the current co-crystals, $LiPF_6$ and Adpn, have
74 been extensively used in liquid or polymeric electrolyte systems. $LiPF_6$ is the lithium salt found in
75 most commercial LIBs despite its poor thermal stability in liquid solution and in pure form. The
76 most studied, more thermally stable replacement salt, LiTFSI, has limited use due to high cost and
77 its corrosion of the aluminum current-collectors for the cathodes[17]. Polar nitrile or cyano-(-C≡N)
78 groups, with high dipole moments and dielectric constants of ~ 30, have been investigated to
79 solvate lithium ions instead of the ether oxygens of polyethylene oxide (PEO) or glymes. Recent
80 reviews have focused on their incorporation as functional groups in liquids, plasticizers, plastic
81 crystals (particularly succinonitrile (SN)[18,19]), gels (e.g., polyacrylonitrile (PAN)[20–29]), PAN
82 polymer-in-salt[30–33] and solid electrolytes used for LIB applications[34]. These materials often have
83 high anodic oxidation potentials (> 4.5 V *vs.* Li^+/Li) and are thus resistant to electrochemical
84 oxidation[35,36] and therefore have the potential to be used with high voltage cathodes[37–39], e.g.,
85 Li[Mn, Ni, Co]O_2. However, these systems lack structural organization and have poor thermal

stability, making high temperature applications impractical. Adpn has also been shown to enable the use of high voltage cathodes when added in small amounts (1%) to other electrolyte solutions, by film formation[40] or strong coordination between the Ni^{4+} on Ni-rich cathode surfaces and the nitrile groups[41]. However, nitriles suffer from poor reductive stability (so that they spontaneously react with Li metal, and stable, conductive solid electrolyte interfaces (SEIs) do not usually form)[36], but can be used with lower-energy anodes such as $Li_4Ti_5O_{12}$ (1.55 V vs Li^+/Li)[19,42], or with graphitic anodes by addition of SEI forming co-solvents[35,43]. More recently, it was shown that low concentrations of Adpn (1%) in mixed electrolytes formed stable SEIs on Li^0 metal[41]. Interestingly, and of importance for the current work, the reductive stability of acetonitrile (AN) was improved in concentrated (> 4 M) salt solutions, since all of the acetonitrile molecules were passivated by coordination to Li^+ ions[44]. In dilute solution, the LUMO is based on AN molecules (coordinating with the Li^+ ions), while in superconcentrated solutions, the LUMO was localized on the TFSI anion instead, preventing reductive degradation of the nitrile.[44]

Here we present the structure, thermal and electrochemical properties of the soft solid crystal of adiponitrile and $LiPF_6$, $(Adpn)_2LiPF_6$, which has an effective molarity of ~ 4.5M. We demonstrate this material has desirable physical properties, including melt- and press-castability, self-healing, high conductivity for an organic solid electrolyte ($\sim 10^{-4}$ $S \cdot cm^{-1}$), and a wide electrochemical stability window of 5 V. Further, it exhibits improved stability over commercial liquid electrolyte solutions by isolating the Li^+ and PF_6^- ions in separate channels.

We constructed lithium metal and lithium-ion cells for cycle testing. Stable cycling was demonstrated for > 50 cycles at C/20, C/10, C/5 rates with capacities of 140 mAh-g^{-1} to 100 mAh-g^{-1} and Coulombic efficiencies > 99% using $Li^o/(Adpn)_2LiPF_6/LiFePO_4$ half-cells and ~ 96%

Coulombic efficiency with LTO/$(Adpn)_2LiPF_6$/NMC622 full cells. The importance of the conduction paths, the role of the interfacial layer, and the distance between Li···Li sites will be discussed.

RESULTS AND DISCUSSION

Structural and thermal characterization

The parent compound $(Adpn)_2LiPF_6$ is prepared by heating commercially available $LiPF_6$ in excess adiponitrile, in which it is sparingly soluble at room temperature[43]. After complete dissolution at 165°C, cooling of the solution yields crystalline material. The X-ray single-crystal structure shows that the stoichiometry is 2 moles of Adpn to 1 mole of $LiPF_6$, $(Adpn)_2LiPF_6$ **(Figure 1a).** In $(Adpn)_2LiPF_6$, there are linear parallel ionic channels of Li^+ **(Figure 1b)**, where the shortest distance between two successive Li^+ ions is 6.23Å in the *b*-crystallographic direction. Each Li^+ ion is coordinated to 4 cyano groups, and does not interact with any PF_6^- anions. The presence of Li^+ channels in a low-affinity matrix is expected to allow facile migration of Li^+. Other dinitrile solvents or other Adpn/LiX form stable solvates at 2/1 molar ratios. These include dinitrile/LiTFSI[45] and the molecular crystal of lithium bis(fluorosulfonyl)imide, LiFSI = $Li(N(SO_2F)_2)$, and succinonitrile (SN), SN_2FSA[12]. For SN_2FSA the closest Li-Li distance in the diamond-like three-dimensional network (space group *P*4*b*2) is 5.03 Å, and the FSA anions also do not interact with Li and are located in the interstitial sites of the disordered diamond-like structure[12].

The experimentally obtained powder X-ray diffraction (PXRD) pattern of $(Adpn)_2LiPF_6$ agrees with the PXRD calculated from the single crystal data **(Figure S1a)**. PXRD data before and after conductivity measurements **(Figure S1b)**, and whether pressed or prepared in a glass fiber mesh

(Figure S1c) are the same. The XRD data show neither the presence of frozen Adpn at low temperature **(Figure S1d)**, nor parent $LiPF_6$. An important consequence of the isolation of the PF_6^- anion from the Lewis acidic lithium is the improvement of the thermal stability of the salt; the thermogravimetric analysis (TGA) data **(Figure S2)** show that the stability of $LiPF_6$ is increased from decomposition temperatures of 100 ºC for pure $LiPF_6$ to > 160 ºC for $(Adpn)_2LiPF_6$ upon incorporation into the co-crystal, such that the stability of the co-crystal is limited by the boiling point of Adpn (Adpn T_m = 1 ^{0}C, T_b = 295 ^{0}C). This is most likely because the segregation of the ions into separate channels prevents the formation of the usual decomposition product LiF. For comparison, the thermal stability of the molecular crystal of SN_2LiFSA was limited to 130 ºC (SN T_m = 57 ^{0}C and T_b = 266 ^{0}C; LiFSI T_m = 142^{0}C; T_2 = 233 ^{0}C for dry salts[46]). It is important to note that T_d of cocrystals of $(Adpn)_2LiPF_6$ is lower than the T_m (**Figure 2a**) due to the continuous removal of Adpn solvent molecules via effervescence with N_2 gas purge during the TGA experiment. However, in a closed system, such as the hermitically sealed pans in DSC measurements, or in a battery cell, the cocrystals show good thermal stability (up to 200 ºC). To model TGA behavior (**Figure S3**), a nanocrystal of electrolytes was simulated in the presence of vacuum (model *V* where "*V*" designates vacuum). This simulation predicts that Adpn molecules evaporate as the cocrystals degrade at high temperature (T > 400 K) **(Figure S3d)**.

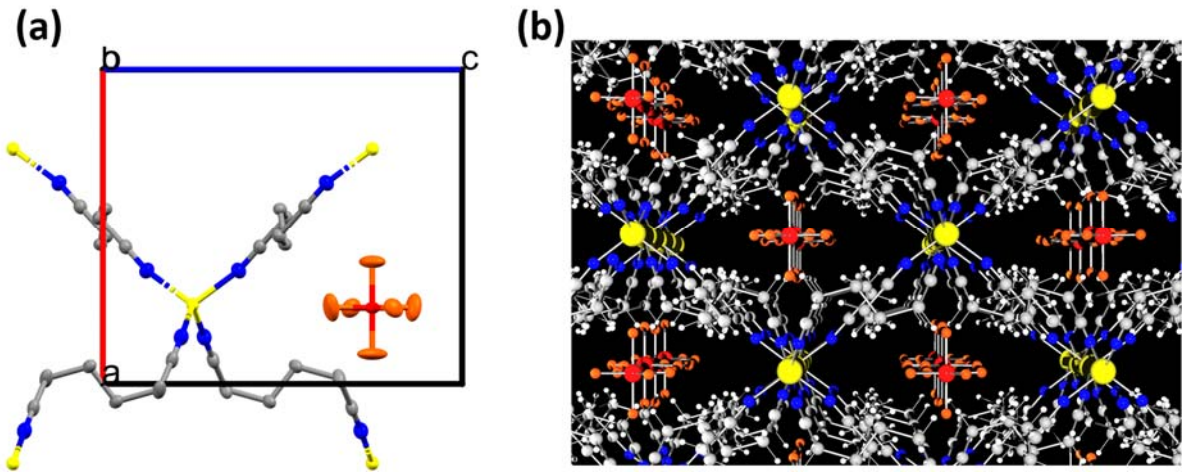

Figure 1. Crystal structure of soft-solid co-crystalline $(Adpn)_2LiPF_6$ electrolyte: (**a**) Representation of the basic structural unit of $(Adpn)_2LiPF_6$ showing tetracoordinated Li^+ ions with four Adpn molecules, each shared with a second symmetry equivalent Li atom, and where PF_6^- anions occupy the available interstitial pocket in the crystal structure; (**b**) Packing diagram of $(Adpn)_2LiPF_6$ showing the channels of Li^+ ions in the low-affinity matrix in the crystal structure. ● Gray- C; ● Yellow- Li; ● Blue- N; ● Red- P; and ● Orange- F.

Differential scanning calorimetry (DSC) data (**Figure 2a**) show that the co-crystals of $(Adpn)_2LiPF_6$ melt at 182 ^{0}C. For comparison, the SN_2FSA molecular crystal melted at T_m = 59.5 ^{0}C[12]. In the case of $(Adpn)_2LiPF_6$, the presence of a small amount of Adpn in the cocrystal was observed (**Figure 2a).** Melting of this Adpn contaminant occurs at approximately the same temperature as for neat Adpn, while crystallization occurs at slightly lower temperatures than neat Adpn, suggesting confinement effects might modulate the heat of fusion. The small amount of free Adpn (i.e., not coordinated to Li^+) in the $(Adpn)_2LiPF_6$ co-crystal is also observed in the Raman spectra (**Figure 2b**). For pure adiponitrile there is only a single peak at 2241.7 cm^{-1}, while for the co-crystal, there is a large peak at 2273.6 cm^{-1} and a very small peak at 2242.7 cm^{-1} slightly red-shifted higher in wavenumber compared with neat Adpn (2241.7 cm^{-1}). Both peaks have been observed in other liquid dinitrile/LiX salts (e.g. succinonitrile/LiTFSI) as a function of LiX concentration.[45], and have been assigned respectively to the coordinated and free "terminal" C≡N

adiponitrile groups[47,48]. In these cases, as the concentration of LiX increases, the lower frequency band increases in frequency compared with the neat dinitriles, and the intensity of the "coordinated" and "free" nitriles bands increases.

Vibrational frequencies calculated using DFT in the gas phase for the molecule shown in **Figure 2c and 2d** (and **Table S1**) are ~ 20-30 cm^{-1} higher in wavenumber than the liquid[45,47] or solid experimental spectra, as also observed for the C≡N mode in similar systems that compared DFT and experimental frequencies.[49] The calculations indicate that the highest frequency occurs when the C≡N groups are coordinated to four Li^+ ions. The lowest frequency occurs when the C≡N groups are uncoordinated with Li^+ ions. However, since the normal vibrational modes are coupled, the decrease in electron density of the N≡C coordinated with Li^+ (C≡N ~~N≡C•••Li^+) results in a migration of electron density away from the uncoordinated ~~C≡N, resulting in an increase in wavenumber in this "uncoordinated" mode. Thus, the 5 cm^{-1} increase in frequency in the experimental Raman spectra for the weak (2242.7 cm^{-1}) vibration compared with that of neat Adpn (2241.7 cm^{-1}) may be due to Adpn molecules at the crystal boundaries, where one C≡N is in the crystal (coordinated to Li^+) and the other end is "dangling" at the interface, and/or to free Adpn with partial coordination to dissolved $LiPF_6$ in the grain boundaries (as is observed for liquids, where this frequency increases with Li^+ ion coordination to C≡N [45,47]).

MD simulations of the solid $(Adpn)_2LiPF_6$ structure may be used to visualize and understand the molecular processes underlying experimentally observed thermal stability properties. Simulations were performed using a bulk phase *periodic* supercell, Model *P*, which consisted of a supercell (125 unit cells, i.e. 20000 atoms) representing the bulk phase of the $(Adpn)_2LiPF_6$ co-crystals. Model *P* was simulated under isothermal isobaric (*NpT*) ensemble conditions for a 20 ns equilibration at different constant temperatures ranging from 100 K to 550

K **(Figure S4).** The equilibrated configurations at 100 K, 200 K and 298 K predict a structured network of tetrahedral Li^+ ions coordinated by Adpn. A visual inspection of snapshots shows that these networks become irregular at 400 K (= 127 ^{0}C) and the crystalline structure completely melts at 500 K (= 227 ^{0}C, **Figure S4**), in agreement with the melting regime observed in DSC data (430 K – 460 K, **Figure 2a)**. The structural analysis from RDFs **(Figure S5)** suggests that the co-crystalline structure changes from completely ordered to solvated/separated ion-clusters in Adpn in the temperature range 450 K - 500 K, similar to the experimental melt temperature of $(Adpn)_2LiPF_6$ from DSC data.

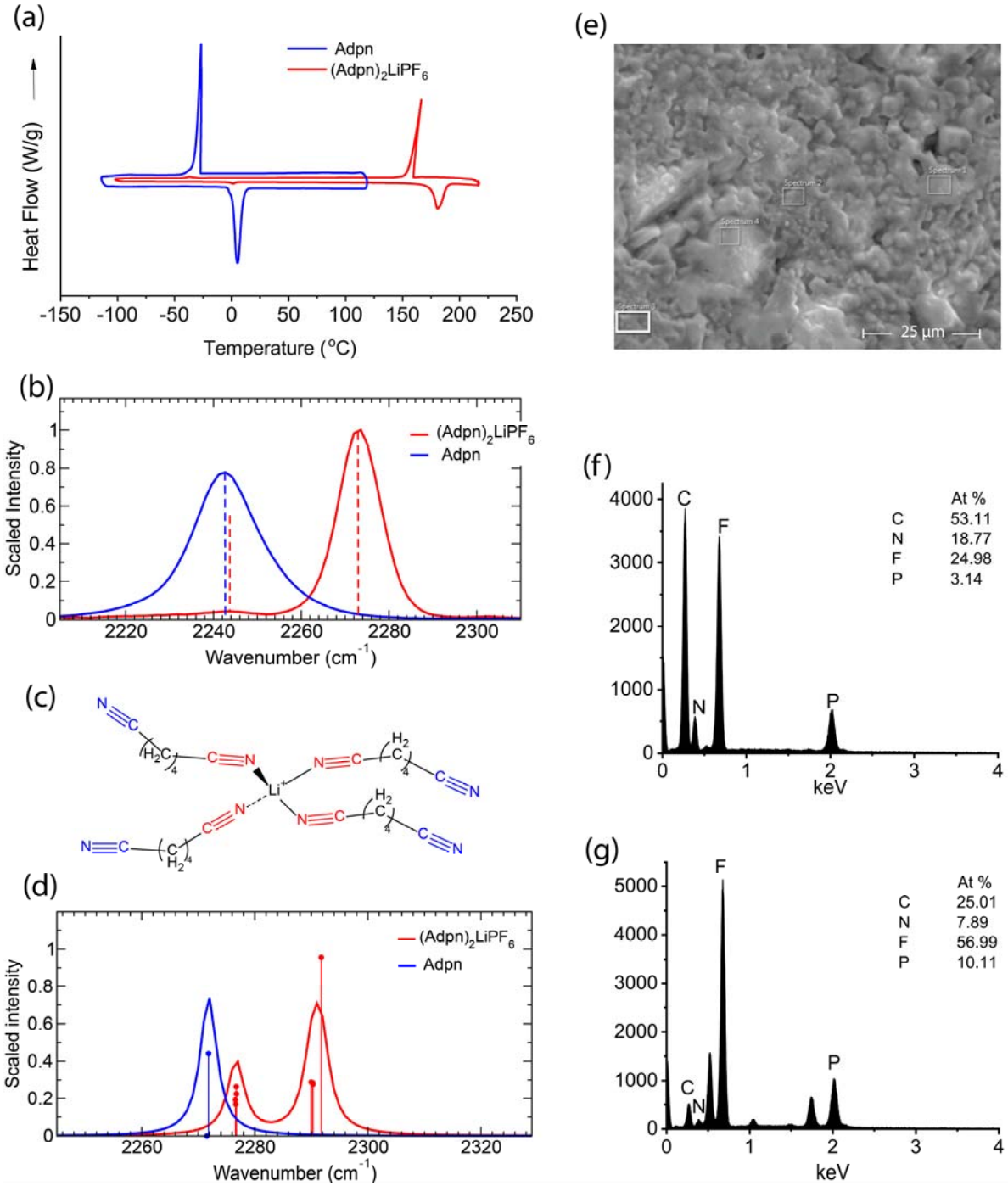

Figure 2. Thermal, structural, and spectroscopic evidence of free solvent molecules at the grain-boundaries of the crystals: (**a**) DSC data of $(Adpn)_2LiPF_6$ (—) and Adpn (—) showing melt and crystallization peaks for both; (**b**) Raman spectra in the -C≡N region from experiment; (**c**) model used for DFT calculations; (**d**) Raman spectra from DFT calculations, where dots are the calculated frequencies and the solid lines are interpolated Gaussian curves obtained by using 1.8 cm^{-1} peak half-width at half height; (**e**) SEM image of pure polycrystalline $(Adpn)_2LiPF_6$

206 powder (pressed neat sample) showing liquid inter-grain binding; **(f)** EDX of bulk grain; and (**g**)
207 EDX of grain boundary regions.

208

209 SEM images were obtained for four samples: 1) a pressed pellet of the polycrystalline
210 $(Adpn)_2LiPF_6$ at RT (**Figure 2e**, **Figure S6**); 2) a sample where the heated solution of Adpn
211 (excess) and $LiPF_6$ was quenched in liquid N_2 and then pressed (**Figure S7**); 3) the polycrystalline
212 $(Adpn)_2LiPF_6$ powder incorporated into a glass fiber (GF) filter by synthesis (illustrated in **Figure**
213 **S8**); and 4) a post-mortem sample of a $Li^0/(Adpn)_2LiPF_6/Li^0$ cell after Li plating/stripping failure
214 (**Figure S9, S10**). The $(Adpn)_2LiPF_6$ crystals - rinsed with diethyl ether - were large, reaching over
215 100 μm in length and ~ 5 μm in width, with rounded edges (**Figure S7, a-c**). These large 100 μm
216 crystals comprise a mosaic structure of smaller, < 1 μm crystalline domains (**Figure S7i**). After
217 pressure was applied, the individual grains fractured into smaller pieces and fused to one another.

218 **Grain boundaries:**

219 EDX images (**Figure 2e,f**) of the grains and grain boundary regions show that the relative C and
220 N X-ray fluorescence peaks of the Adpn are weaker compared with the F and P peaks of the $LiPF_6$
221 in the grain boundary region than in the grains. This suggests that the grain boundary region is
222 fluid, and that under the vacuum of the SEM, the Adpn is evaporated, leaving behind concentrated
223 $LiPF_6$ salt. Such surface liquid phases are well known and are due to a decrease in lattice energy
224 for molecules near the surface of crystals, and most famously illustrated by the surface liquid water
225 layer in ice.[50] A nanocrystal of this electrolyte was simulated in the presence of vacuum (model *V*)
226 predicting that Adpn molecules evaporate as the cocrystals degrade at high temperature (T > 400
227 K) (**Figure S3d**). In addition, model *V* also shows that the cocrystals at room temperature possess
228 a liquid-like surface layer (**Figure S3b**) similar to other soft solid cocrystals[16], and which is also

seen from SEM analysis of this electrolyte (**Figures S6 and S7**). This nanoliquid surface behavior is a general characteristic of this class of electrolytes[13,14,16,51].

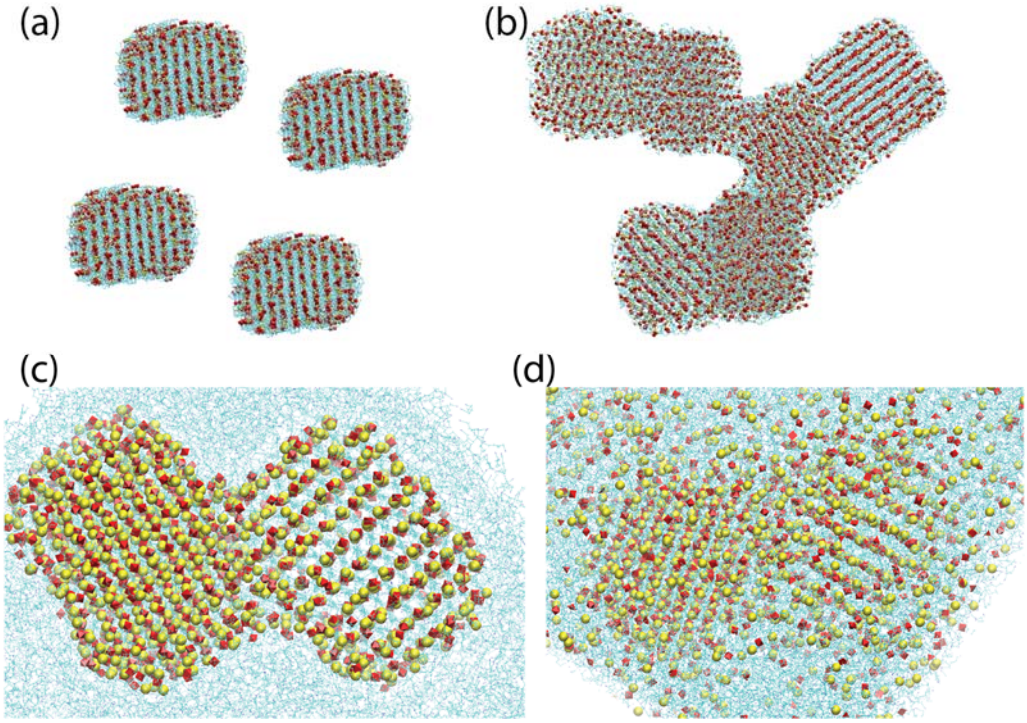

Figure 3. Simulation of model vacuum models V_{8g} and $V_{2g,sol}$ of $(Adpn)_2LiPF_6$ (total 160000 atoms and 140576 atoms, respectively): (a) Initial condition of model V_{8g}, only the four grains in the front are visible, the other four grains are behind, (b) model V_{8g}, after a simulation time of 10 ns, under NVT ensemble, (c) model $V_{2g,sol}$ – where two grains of $Adpn_2LiPF_6$ are solvated with 6286 molecules of Adpn to model grain boundaries, after initial equilibration of 5 ns, (d) model $V_{2g,sol}$ after 15 ns production run.

To determine the structure of the intergranular interface, model V_{8g} (surface model) with eight nano-sized grains (1 grain = 5x5x5 unit cells) was simulated in a vacuum box of 30x30x30 nm^3 **(Figure 3a)**. The simulation conditions of model V_{8g} were very similar to model *V* (e.g., *NVT* ensemble, presence of large evacuated space). At $t = 0$, it was ensured that every grain was completely isolated from the others (initial contact distance between the grains > cut-off distances for potential energy). The simulations show that within a span of a few nanoseconds, the grains

interact at the surface and form a more mobile interfacial layer **(Figure 3b, Supplementary Movie 1)**. This interfacial layer does not depend on the orientation of the grains or the size of the box, which implies that the formation of an intergranular interface does not require lattice matching. The formation of the interface in the V_{8g} model, despite its inclusion of multiple grains with interfaces, does not simulate the formation of such interfaces under experimental conditions since V_{8g} occurs in a vacuum. During synthesis, Adpn solvent molecules are trapped/confined between the grains and form part of the grain-boundaries. To simulate this effect, two grains of $Adpn_2LiPF_6$ were solvated with 6286 Adpn molecules and modelled ($V_{2g,sol}$) using two grains that were kept at a distance of 1.5 nm (> 1.4 nm cut-off distance used for the search of neighbor and calculation of forces). After an equilibration of 5 ns at room temperature, the model $V_{2g,sol}$ shows initial inter-phase contact between the two grains **(Figure 3c)**. A 20 ns production run under *NVT* conditions shows that several Li^+ and PF_6^- ions from the crystal dissolve in the free Adpn solvent molecules **(Figure 3d)**. The presence of disordered ions at the fluid interface can facilitate grain boundary conduction since ion jumps across the grain interface are not required in these regions due to high mobility, in contrast to ceramic organics, whose grains must be sintered to prevent insulating inter-grain gaps. The dynamics of ions in these inter-grain regions is discussed in the section **Mechanism of Ion transport**.

Electrochemical testing:

The electrochemical impedance spectroscopy (EIS) data **(Figure 4a)** for a pressed pellet of $Adpn_2LiPF_6$ in the temperature range between -10ºC and 80 ºC (below its degradation temperature), show a RT conductivity of $\sigma \rightarrow 10^{-4}$ S cm^{-1}, with an Arrhenius activation energy of $E_a = 37.2$ kJ mol^{-1}. The complex impedance spectra were analyzed using a constant phase-element resister (CPER)/constant phase-element (CPE) circuit **(Figure S11b)**.

The variation of the DC current as a function of time **(Figure S11a),** in a Li(s)/Li(s) cell, including the correction for the interfacial resistance before polarization (R_0) and steady-state (R_s):

$$t_{Li^+} = \frac{I_S(\Delta V - I_0 R_0)}{I_0(\Delta V - I_0 R_S)})$$

gave a lithium-ion transference number of $t_{Li^+} = 0.54$. Unlike inorganic ceramics with a stationary anion lattice and mobile Li^+ sublattice ($t_{Li^+} \rightarrow 1$), here both the anions and cations are mobile, but with a better t_{Li^+} than in typical commercial liquid electrolytes.[52]

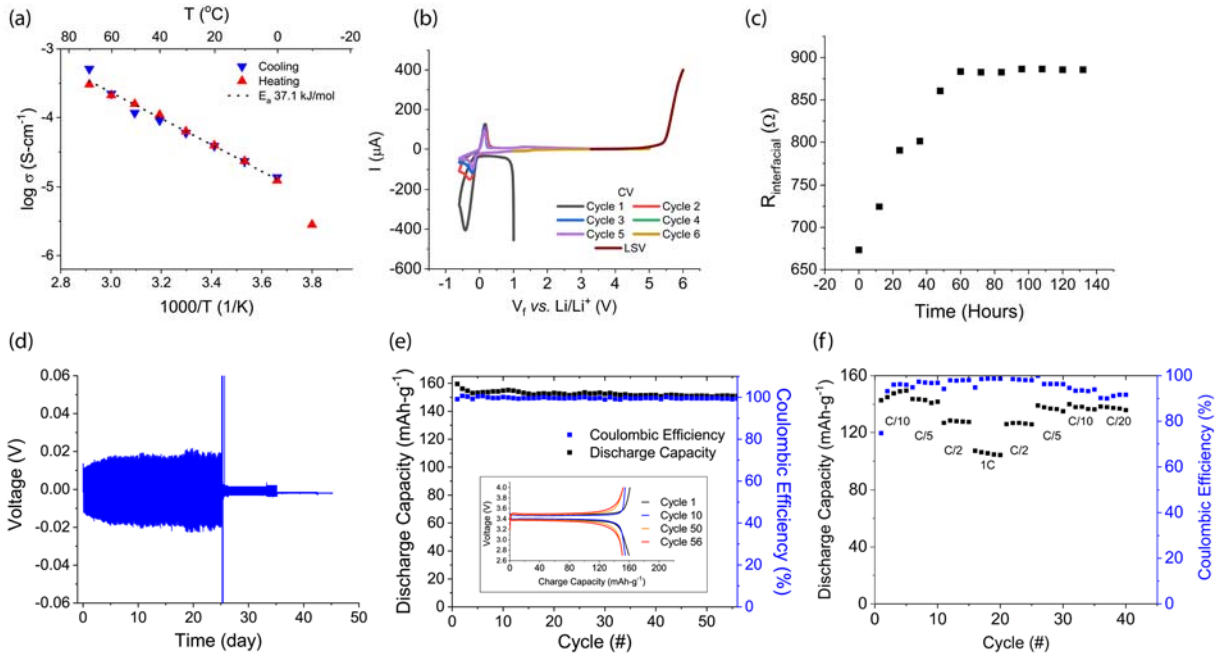

Figure 4. Electrochemical data on $(Adpn)_2LiPF_6$: (a) Variable temperature conductivity data of a pressed neat pellet of SS/$(Adpn)_2LiPF_6$/SS; model CPE circuit diagram is provided in **Figure S11b**; **(b)** CV and LSV of Li^0/$(Adpn)_2LiPF_6$/SS, with $Adpn)_2LiPF_6$ synthesized in glass fiber; **(c)** Interfacial resistance as a function of time in Li^0/$(Adpn)_2LiPF_6$/Li^0 cells using $(Adpn)_2LiPF_6$ in glass fiber separator at room temperature, taken before cycling; **(d)** Li plating, 2 h charge/discharge cycles at J = 0.01 mA/cm^2 for 120 cycles, J = 0.05 mA/cm^2 for 60 cycles and J = 0.1 mA/cm^2 for 60 cycles with a zoomed-in version provided in **Figure S11c and d**; same cell as in (**c**); **(e)** Discharge capacity and Coulombic efficiency as a function of cycle number in Li^0/$(Adpn)_2LiPF_6$/$LiFePO_4$ cell at C/10 rate at 25 ^{0}C; inset shows the voltage *vs.* charge capacity for cycle # 1, 10, 50 and 56; and (**f**) Capacity and Coulombic efficiency of LTO/$(ADN)_2LiPF_6$/NMC622 cells at 25 ^{0}C as a function of C-rate, with no conditioning cycles.

Capacity and Coulombic efficiency at C/10 rate as a function of cycle number, 2h charge/2h discharge with two cycles of preconditioning at C/40 rate is provided in **Figure S11e.**

Adpn has excellent oxidative stability[43,53], and based on LSV, the oxidation current begins to increase only at 5V vs. $Li^0|Li^+$ **(Figure 4b)**. Normally, Li metal is thermodynamically unstable with almost any organic solvent, leading to side reactions that consume both Li metal and the electrolyte[54]. However, a piece of Li^0 metal placed in Adpn (with or without $LiPF_6$, which has minimal solubility at RT) is much more resistant towards reaction than when placed in acetonitrile (AN). It remains shiny for several days, and the solvent remains colorless for weeks to months (**Figure S12**). By contrast, when Li metal was placed in dilute LiTFSI/AN, the Li metal quickly dissolved, and the solution turned yellow[44]

Adpn is known to be thermodynamically unstable at low potentials (~ 0.6V vs Li/Li^+) [55], as is acetonitrile (AN). However, nitrile solvents are stabilized with respect to reaction with lithium metal in the presence of concentrated salts.[43] Reversible Li^0 stripping/plating is observed for $(Adpn)_2LiPF_6$ (**Figure 4b**), which has an effective molarity of 4.5M, while in dilute AN/LiTFSI (<3M) Li stripping is not observed[44]. In the CV scans, during repeated lithium stripping, the oxidation peak at ~ 0.5 V (vs Li^+/Li) superimposes onto itself, while during lithium plating, the reduction peak at ~ - 0.5 V decreases from the 1st through the 3rd cycles and then remains stable. This suggests that a stable, ionically conductive SEI layer is being formed during the first three cycles. Interfacial resistance **(Figure 4c)** in a $Li^0/(Adpn)_2LiPF_6/Li^0$ cell stabilized at about 900Ω after 3 days. Lithium plating in the same cell **(Figure 4d)** was stable for 20-25 days at low current densities (J = 0.01 mA/cm^2) but failed at higher current densities

The reactions at the Li surface during Li cycling are determined by the thermodynamic electrochemical stability window of the electrolyte, which is dominated by the frontier orbitals (HOMO and LUMO) of the salt and solvent[56]. During the cathodic scan (lithium plating), electrolyte components are reduced and deposited on the Li metal to form the solid electrolyte interface (SEI) layer. In the electron rich environment of the anode, the SEI will be formed by the component that is most easily reduced (i.e., the component with the lowest-energy LUMO). Qualitatively, interaction/association of a solvent or anion with Li^+ lowers the energy of the ligand LUMO, such that the ligating species is more easily reduced. In concentrated LiX solutions, contact ion pairs have lower LUMOs than solvated Li ions, which results in preferential reduction of the anion[57]. In $(Adpn)_2LiPF_6$, however, the Li^+ ion is solvated by the Adpn (as shown from its crystal structure) with no contact ion pairs, which suggests Adpn to be more easily reduced, and thus forms the SEI. This is predicted quantitatively for $(Adpn)_2LiPF_6$ in **Figure S13**, where projected density of states (DOS), obtained from plane-wave DFT calculations, show that after addition of an electron, the bandgap decreases and the LUMO is located on the Adpn carbon atom. Further confirmation that the reduction reaction occurs predominantly on Adpn, comes from differential electron density maps (**Figure S14**), which show that addition of an electron changes the electron density close to C≡N (Adpn) compared with the PF_6^- anion.

Further, the absence of free solvent has also been suggested to mitigate the reductive decomposition by affecting an upward shift in the equilibrium potential of the Li electrode (as the result of the increased mole fraction of Li^+ (x_{Li}) and higher γ_{Li}, since the solvent acts as part of the solute, ($E = E^0 + \left(\frac{RT}{F}\right) ln(x_{Li}\gamma_{Li})$)) and to increase the stability of the SEI, by the lack of solvent to dissolve the SEI[57]. As discussed later in the mechanism of Li^+ ion conduction, in the $(Adpn)_2LiPF_6$ cocrystals the cyano groups of Adpn do not undergo long range migration during

the conduction process, and thus there is not continual replenishment of Adpn to the Li^0 metal surface, and as a result, there is a cessation of SEI formation after a few cycles. It is also possible that the Adpn from the grain boundaries is polymerized to form a protective SEI during cathodic polarization as recently proposed for Adpn[58] and for acetonitrile (forming polyacrylonitrile).[59]Cycling data was obtained for Li^0/$(Adpn)_2LiPF_6$/$LiFePO_4$ half-cells and LTO/$(Adpn)_2LiPF_6$/NMC622 full cells. Excellent cycling data was obtained for the half cells at C/20, C/10, and C/5 rates (~ 140 mAh^{-1}/g) with little capacity fade (**Figure S15a and b**) between 2.7 and 4 V. The C/10 data ran for > 70 cycles (56 shown) before capacity fade (**Figure 4e**). These results compare favorably with results obtained in related previous studies with liquid Adpn/1 M salts, where only 20 cycles were obtained with efficiencies of ~ 97%.[60] Thus, the highly concentrated $Adpn_2LiPF_6$ improves compatibility with the Li^0 metal.

Full cell with LTO/$(Adpn)_2LiPF_6$/NMC622 were studied to investigate the potential for these electrolytes to be used with high voltage cathodes. LTO was selected since a stable and conductive solid electrolyte interphase (SEI) is not formed on graphite[61] and LTO has a charge plateau at 1.55V vs. Li/Li^+. Lithium manganese cobalt oxide ($LiNi_xMn_yCo_zO_2$ with x + y + z =1), NMC, cathodes are currently the most viable high voltage candidates, and NMC622 was used here. The C-rate performance of LTO/$(Adpn)_2LiPF_6$/NMC622 cells is presented in **Figure 4f**, and the cycling performance at C/10 shown in **Figure S11e**. The cells were cycled between 2V and 4.2V vs Li/Li^+. The theoretical capacity of the cells was 160 mAh/g. (The theoretical capacity of the cells is based on what was given by the manufacturers, 160 mAh/g for NMC-622, ~161 mAh/g for LTO). The accessible capacity decreased with C-rate, as expected, but recovered when returned to the original C-rates. For cells cycled at the C/10, there was capacity fade of ~ ½ over 100 cycles, but no catastrophic failure (see **Figure S11e**). Further, the Coulombic efficiency was steady at ~

96% for the whole 100 cycles. This compares favorably with previous studies, in liquid Adpn/1M LiX and MCMB/$LiCoO_2$ full cells, where there was a mere 0.1% remaining capacity after only 50 cycles and none after 100 cycles, and additives (5% vinyl or monofluoroethylene carbonate) were required to improve capacity retention to 86%.[62] In lithium titanate ($Li_4Ti_5O_{12}$, LTO) anodes and high voltage cathodes Li Ni Co Mn O_2 (NMC), specific cell capacities of 165 mAh/g were obtained only at low rates (C/10) in liquid Adpn/LiTFSI electrolytes[47]. It is well known that the Ni in NMC cathodes reacts gradually with electrolytes, and the $Adpn_2LiPF_6$ is no exception. NMC622/$(Adpn)_2LiPF_6$/NMC622 cells (**Figure S15d and e**) show increases in impedance from 800Ω to 950Ω over 5 days. However, these are properties of the anode, not the electrolyte, and the results demonstrate the ability of $(Adpn)_2LiPF_6$ electrolytes to be used with high voltage cathodes. Comparison of the Li^0/ Li^0, Li^0/$LiFePO_4$, LTO/NMC622 and NMC622/NMC622 cells suggests that both the anodes and cathodes contribute to capacity fade, with comparable impedances for both anodes and cathodes.

Post-mortem analysis:

The ideal properties of an SEI are that it is thin, flat, electrically insulating (to suppress further reductive decomposition), and ionically conductive. Interfacial resistance **(Figure 4c)** in the Li^0/$(Adpn)_2LiPF_6$/Li^0 cell stabilized at about 900Ω after 3 days. Lithium plating in the same cell **(Figure 4d)** was stable for 20-25 days at low current densities (J = 0.01 mA/cm^2) but failed at higher current densities. Post-mortem analysis showed that the Li surface was black. SEM images (**Figure S9**) indicate that the SEI was rough (not flat) with a thickness < 5 μm after ~ 30 days, suggesting a compact but mossy SEI layer, with no obvious dendritic growth. EDX analysis (**Figure S10**) of the surface showed residual $(Adpn)_2LiPF_6$ crystals that adhered to the SEI layer, based upon their morphology and dominant C, N, F and P signals, with little or no O. At the SEI

layer itself, the major peaks were O (from Li_2O) and C (from Adpn), with very little P and F (from PF_6^-). While further investigation is required, these peaks suggest the formation of lithium oxides and carbonates. The formation of compounds containing C (such as carbonates), and the scarcity of F, P, agree with predications from electronic structure calculations that the Adpn reduction could cause solvent degradation leading to SEI layer formation at the Li^0 anode.

The drop in cell voltage at the higher current densities may be the result of Li dendrites so thin as not to be easily observable by post-mortem analysis, and which leak only a small amount of current. One hypothesis is that the dendrites grow in the nanoliquid grain boundaries of the $(Adpn)_2LiPF_6$ cocrystals. Support for this hypothesis comes from cycling data (**Figure S15 a and b**) on two half-cells: Cell 1 **(Figure S15a)**, studied at RT, which fails at C/2 rate, and cell 2 **(Figure S15b)**, at 10 ^{0}C, which survives cycling at 1C rate and recovers. The failure of cell 1 and recovery of cell 2 can be attributed to: at 25 ^{0}C, the grain boundary region is more mobile, allowing Li^+ ion mobility and dendrite growth causing cell failure, while near the freezing point of the "free" or interstitial (half Li coordinated and half free) Adpn, Li^+ ions cannot migrate which prevents both charging/discharging, as well as dendrite growth.

Mechanism of ion transport

The mechanism of conduction of Li^+ in $(Adpn)_2LiPF_6$ co-crystals is of interest. For polymer electrolytes above T_g the diffusion of the Li^+ ions is coupled to the slow backbone dynamics of the polymer chain[63]. In organic solvents, there is a vehicular diffusion mechanism of solvated Li ions[64]. In both cases, the fluidity of the matrices often results in linear diffusion and MD simulations become useful for the calculation of the diffusion coefficient, *D*. In the cases where polymer electrolytes solidify, a high temperature MD simulation is often used to estimate ion

mobility precisely. Inorganic solid electrolytes (e.g., LISICON, garnets) usually possess a strongly bonded, thermally stable sublattice of the anionic component of the electrolyte, and a mobile sublattice of Li^+ ions. The fixed anionic sublattice in LISICONs enables modeling of Li^+ ion diffusion- as MD simulations can be performed at sufficiently high-temperatures without destroying the sublattice matrix leading to good jump statistics even at small timescales.

In contrast to other solid electrolytes, our family of co-crystalline electrolytes does not possess a stable anionic sublattice and/or fluidity at high temperatures, which pose serious limitations on the implementation of simulation methods; e.g. *NVT* simulations on Model *P* did not show ionic jumps even at long timescales (**Figure S16**), nor did an analysis based on calculations of the self-part of van Hove autocorrelation function (vH ACF)[65] (**Figure S17)**. To address these challenges, we perform high-temperature molecular simulations along with introduction of ionic defects to model ionic diffusion in the $(Adpn)_2LiPF_6$ cocrystals (Model *D*). This approach provides improved jump statistics and enables understanding of ionic diffusion from classical simulations. MD simulations on defected supercells (model *D*) were employed where four vacancy sites of cations and anions were created, each at random places in the supercell (two defects were at least 1.5 nm away from each other in order to prevent any initial interactions among vacancy sites). Further, we simulated model *D* for a timescale of 50 ns at 400 K and for 20 ns at 450 K under *NVT* ensemble conditions. For the simulations on model *D*, the trajectory was recorded at every 5 ps to obtain trajectory maps (**Details in SI and Figure S18**).

At T = 400 K **(Figure S18a-c)**, the map shows that Li^+ ions jump to the interstitial sites and occupy the vacancy sites. Between 30 to 40 ns **(Figure S18d)**, a few interstitial jumps for Li^+ ions were observed in the cocrystals. At 450 K **(Figure S18e-g)**, the interstitial jumps are observed more

frequently compared to those at 400 K. However at t > 10 ns, the structure collapses at 450 K – suggesting decomposition of the bulk at a lower temperature ($T_{d,sim}$ = 475 K from model *P*) due to the presence of vacancy sites. The MSD *vs.* time plot for model *D* at 400 K **(Figure S19a)**, shows that the Li^+ ions remain trapped and only a few jump events are probable at these timescales. Since PF_6^- anions are not present in a confined environment as are the Li^+ ions, the initial oscillations that cause ballistic diffusion are larger in PF_6^- compared to Li^+.

At T = 450 K, just below the melt temperature, the trajectory maps show a significant number of jump events **(Figure S18e-g),** so that diffusion coefficient and Li ion transference numbers can be calculated. PF_6^- anions are not present in a confined environment as are the Li^+ ions, so the initial oscillations that cause ballistic diffusion are larger in PF_6^- compared to Li^+. At T = 450 K, linear diffusion for Li^+ and PF_6^- ions is observed even at very short timescales **(Figure S19b)**. The MSD is calculated for both Li^+ and PF_6^- ions for a trajectory of 20 ns, where the Li^+---N cages break and various sublattices become completely mobile after 10 ns. Thus, the diffusion coefficients for Li^+ and PF_6^- ions were calculated for two different time intervals: 0 – 10 ns and 10 – 20 ns. From 0 – 10 ns, D_{Li^+} = 1.32(4) x 10^{-6} cm^2/sec and $D_{PF_6^-}$ = 1.00(5) x 10^{-6} cm^2/sec, while from 10 – 20 ns, D_{Li^+} = 1.21(3) x 10^{-6} cm^2/sec and $D_{PF_6^-}$ = 1.02(4) x 10^{-6} cm^2/sec. For the interval 0 – 10 ns, the calculated transference number for Li^+ ions is, t_{Li^+} = 0.57, and for the interval 10 – 20, t_{Li^+} = 0.54, in good agreement with the experimentally determined value of 0.54.

Since the $Adpn_2LiPF_6$ electrolyte has a fluid surface region and contains Adpn solvent between the co-crystalline grains—possibly as a nano-confined liquid—the mechanism of ion transport is along the grain boundary and interstitial regions is expected to be significant, with an additional contribution from the motion of ions inside the bulk cocrystal. We believe that the ion

conduction is more facile in the grain-boundaries owing to their liquid like nature and the disordered regions at the co-crystal surface, which leads to the formation of defects at the crystal surface that may perpetuate inside the bulk cocrystal. Hence the net ion conduction can have at least these two contributions – at the grain-boundaries of the cocrystals and inside the cocrystal where vacancies form. Hence the ionic conductivity should have at least two E_a barriers from these two contributions and the effective ionic conductivity (observed in experiments) can be expressed as:

$$\sigma_{eff} = \sigma_{0,eff}\, e^{-\frac{E_a}{RT}} = \sigma_{bulk} + \sigma_{gb} \quad (1)$$

where

$$\sigma_{bulk} = \sigma_{0,bulk}\, e^{-\frac{E_{a(bulk)}}{RT}} \quad (2)$$

and

$$\sigma_{gb} = \sigma_{0,gb}\ e^{-\frac{E_{a(gb)}}{RT}} \quad (3)$$

In order to address these two important contributions, we calculated the MSD for 1000 Li^+ ions in the $V_{2g,sol}$ model (where two grains are simulated in the presence of excess 6286 molecules of Adpn, corresponds to $Adpn_{8.2}LiPF_6$). The $V_{2g,sol}$ model was simulated for 15 ns under *NpT* conditions for thorough equilibration to see the convergence of density and then for another 20 ns under *NVT* conditions. The model was simulated at three temperatures, 300, 325 and 350 K to calculate the MSD of the ions. **Figure 5a-c** show the position overlapped trajectory maps for Li^+ ions in last 5 ns of the production run with every frame recorded at 5 ps at 300, 325 and 350 K. The trajectory maps show that at 300 K **(Figure 5a)**, significant number of surface ions diffuse

to the solvent region, while the bulk region remains intact. At 325 K, some more Li^+ ions from surface become diffusive to the solvent region **(Figure 5b)**, and at 350 K all Li^+ ions become mobile as the grains attain complete solvation **(Figure 5c)**. The equilibrated density for model $V_{2g,sol}$ at these temperatures is provided in **Figure S20.** The individual MSDs are calculated for every (of the 1000) Li^+ ion in both the interior and the surface of the co-crystals to check the spread of ionic mobility. The calculated MSDs *vs.* time plots for individual Li^+ ions at 300, 325 and 350 K are shown in **Figure 5d-f** as green color thin lines. The average MSD for all the Li^+ ions is shown as thick dotted lines. The thick line includes contributions from both bulk and surface diffused Li^+ ions. Plotted at log-log scale, the MSD *vs.* time plot for individual Li^+ ions show two major groups with low and high MSDs and some ions in between those, at 300 K **(Figure 5d)**. The ions falling in these groups belong to the bulk (ordered and less mobile) and the surface (highly mobile) part of the crystals, also seen in the trajectory map at the same temperature **(Figure 5a)**. While the group of ions with lower MSDs show sub-diffusive behavior, as expected for the ions in the bulk, the ions at the surface are solvated by the excess solvent molecules and are linearly diffusive. The purpose of this model ($V_{2g,sol}$) is to compute diffusion with both the contributions, and thus the red-dotted line includes contribution from all the 1000 Li^+ ions. At 325 K, more ions show higher MSDs in the plot **(Figure 5e)** which suggest that more ions become solvated from the surface and less of the bulk-ordered structure is remaining (also visible in **Figure 5b**). At 350 K, the individual MSDs which were spread over a wide range on y-axis become narrow **(Figure 5f)**, as if all the Li^+ ions now correspond to a single group – surface-solvated ions. This suggests that the crystals are solvated at this temperature due to the presence of excess solvent molecules. The calculated average diffusion coefficients Li^+ ions are presented in **Table S2 of the Supporting Information**.

The motion of the ions present in the bulk contributes as σ_{bulk} with an activation energy barrier of $E_{a,bulk}$ to the net ionic conductivity. Since this barrier is impossible to calculate with MD simulations, we have performed NEB calculations in pw-DFT framework discussed in the subsequent section. The Li^+ ions present at the grain surface diffuse in the Adpn solvent boundaries and contribute as σ_{gb} to the net ionic conductivity, with an activation barrier of $E_{a,gb}$. For σ_{gb} the diffusion coefficients are computable if the exact concentration of the Li^+ ions in the grain boundaries is known. The $V_{2g,sol}$ model provides an average value of D_{Li^+}which takes into account the contribution from both bulk and grain-boundary ions **(Table S2)**. To separately estimate the two-barriers (for σ_{bulk} and σ_{gb}), we performed MD simulations with a model which contains 40 $LiPF_6$ molecules solvated with 216 Adpn molecules. This concentration is an estimate based on a compromise between the low solubility of $LiPF_6$ in Adpn (0.04M) and the high concentration of $LiPF_6$ in the co-crystal (4.6M). The calculated diffusion coefficients for a 1.7 M solution of $LiPF_6$ in Adpn are provided in the **Table S2** of the **Supporting Information**. The calculated D_{Li^+} in $V_{2g,sol}$ and a 1.7 M solution are fitted to the Arrhenius equation **(Figure 6a)**. The calculated E_a barriers and their interpretation are as follows: i) The calculated E_a from $V_{2g,sol}$ model considers all the Li^+ ions present in both the bulk and surface region, hence this E_a should be comparable to the experimental E_a from impedance measurements (37 kJ-mol^{-1}); ii) The calculated E_a from 1.7 M solution corresponds to a rough model of grain-boundary solvated Li^+ ions and considers all the Li^+ ions present in a nano-confined environment of Adpn, and is thus comparable to $E_{a,gb}$; iii) Since diffusion in only the bulk is not calculable due to highly non-linear diffusion, the $E_{a,bulk}$ is calculated from NEB-DFT calculations later (see below). The calculated E_a barrier from the $V_{2g,sol}$ model is 44 kJ-mol^{-1} which is slightly higher than the experimental $E_{a,exp}$ (37 kJ-mol^{-1}). The $E_{a,gb}$ is 27 kJ-mol^{-1}, which suggests that the most of the conduction occurs via grain boundaries.

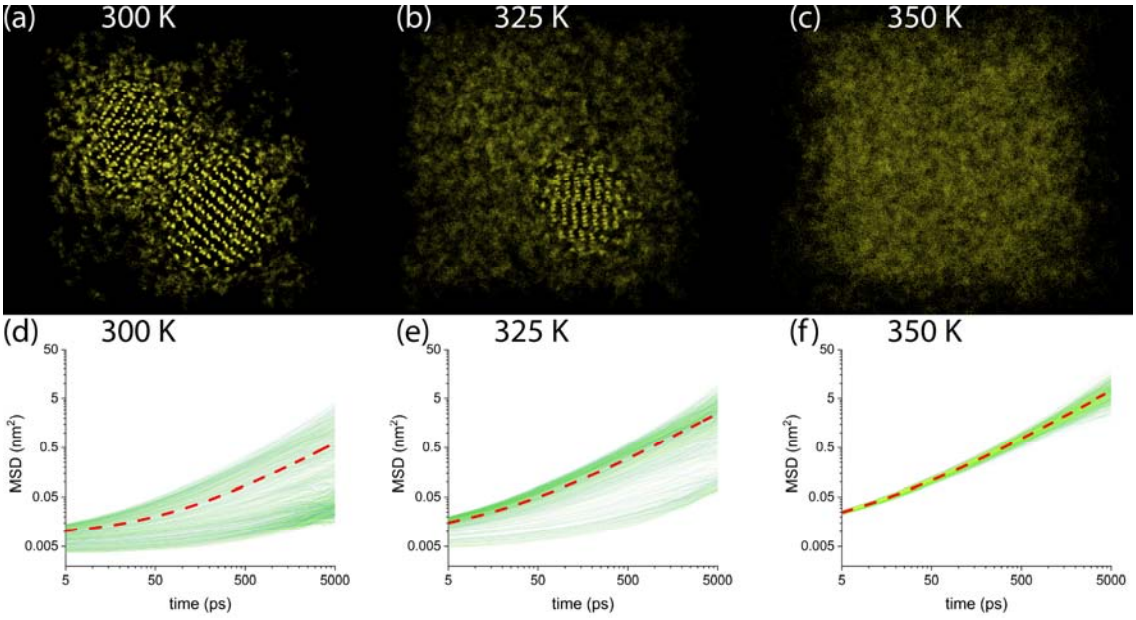

Figure 5. Trajectory maps for 1000 Li^+ ions simulated as model $V_{2g,sol}$ where the position of each Li^+ ion is recorded every 5 ps and overlapped for 5 ns of production run to visualize movement of Li^+ ions: at **(a)** 300 K, **(b)** 325 K and **(c)** 350 K. **MSD *vs.* time plot for Li^+ ions in model $V_{2g,sol}$:** at **(d)** 300 K, **(e)** 325 K and **(f)** 350 K, the distribution of MSDs is for each individual Li^+ ion is shown as green colored thin lines. The averaged MSD for all Li^+ ions is shown as a dashed red line.

Mechanism of ion conduction from DFT:

An atomistic mechanism from DFT is presented that quantifies the longevity of interstitial jumps and feasibility of jumps to the vacancy sites, and provides the barrier $E_{a,bulk}$ from NEB calculations. In the unit cell of $(Adpn)_2LiPF_6$, the shortest possible distance between successive Li^+ ions is 6.6 Å (6.3 Å from XRD) which is parallel to the *b* crystallographic direction **(Table S3, Figure S21)**. To examine all the possible Li^+ migration channels, several different supercells were created. For these supercells, one Li^+ ion vacancy site was created to calculate the minimum energy path (MEP) of Li^+ ion migration between adjacent occupancy sites. The defected supercell images (images: where the defect is located at a different site in the same supercell) were optimized in a fixed volume cell. Various pairs of reactant and product were used to examine the MEP for Li^+ ion

migration using NEB calculations. The extrapolation of Li^+ ion migration paths and calculated activation energy barriers suggested the channel in the *b*-crystallographic direction (Li^+-Li^+ = 6.5 Å) to be the one with the lowest energy **(Figure 6b)**. Hence, further results are discussed for this particular case only, while the information about the other paths is provided in the **Supporting Information**.

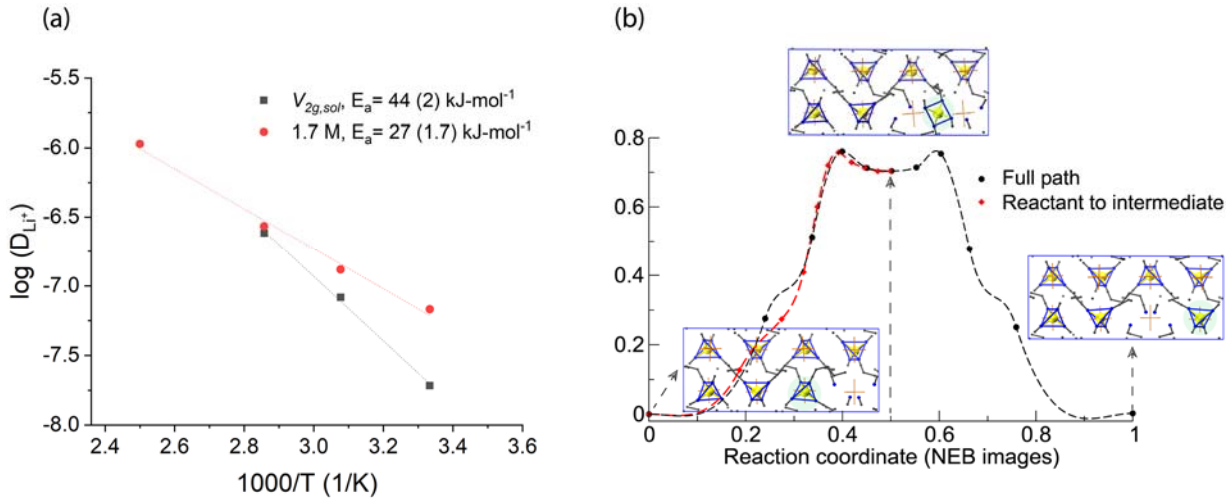

Figure 6. (a) Arrhenius plot for diffusion coefficients of Li^+ ions from $V_{2g,sol}$ model and 1.7 M solution. The E_a barriers from a linear fit are provided with the legends. **(b)** Minimum energy path (MEP) for Li^+ ion migration in the bulk, in *b*- crystallographic direction, as observed from a 1x2x1 supercell of $(Adpn)_2LiPF_6$: The geometries of initial, final and intermediate structures are shown above. The location for migrating Li^+ ion can be seen in the highlighted spot. A dynamic visualization of the Li^+ ion migration is presented in Supplementary movie 2.

The Li^+ ions form a sterically unblocked array parallel to the *b*-crystallographic direction with a short distance between the Li^+ ions, and with no interstitial PF_6 anions, in contrast to the paths in the *a*- and *c*- directions. This results in the possibility of a low barrier migration path for the Li^+ ions in this direction. The calculated path of the Li^+ ion in the *b*-direction shows migration of Li^+ ions from one occupancy site to a vacancy site via an intermediate **(Figure 6b, Supplementary Movie 2)**. When a Li^+ ion defect is introduced in the supercell, the nitrogen atoms of Adpn molecules repel one another and vacate the Li site to stabilize the vacancy. While the

regular N···N distance in Li^+---N networks is 3.2 to 3.4 Å, the presence of a vacancy site increases this distance from 3.6 Å to 5.4 Å. A set of 11 intermediate images was used to extrapolate the path of the Li^+ ion. The climbing image-NEB calculations suggest that a Li^+ ion migrates via the formation of an intermediate structure just between the two Li^+ occupancy sites along the *b*-crystallographic direction. The MEP was calculated for initial and intermediate images separately (11 images). The geometry of the intermediate structure is a Li^+---N tetrahedron, which forms with a reorientation of two of the four Adpn molecules from each end. When the intermediate forms, the remaining two Adpn molecules appear to be a part of an elongated tetrahedron. The intermediate structure (relative energy = 0.70 eV = 67 kJ/mol) has two transition state structures at either side of the reaction coordinate with a barrier of 0.75 eV (= 72 kJ/mol).

This activation energy, $E_{a.bulk}$, is approximately two times larger than $E_{a,exp}$. The occurrence of an intermediate structure also predicts that there is no involvement of anions during the cation transport, contrary to what has been observed in a similar class of sodium ion electrolyte $(Adpn)_3NaClO_4$, where both anion and solvent coordinate with the cation leading to the formation of a transition state[16]. The calculated E_a barriers from various theoretical and experimental methods ($E_{a,exp}$ = 37, $E_{a,MD}$ = 44, $E_{a,bulk,DFT}$ = 72, $E_{a,gb,MD}$ = 27, all in kJ-mol^{-1}) suggest that the most feasible path for Li^+ ions is diffusion via grain boundaries. This mechanism facilitates the initial diffusion in the interstitial region, which then can produce more defects in the few outer layers of the cocrystals leading to sophisticated jump events. The complete understanding of mechanism will require study of more control models in future. However, it should be noted that the experimentally determined solubility of $LiPF_6$ in Adpn (whether directly dissolved or by dissolution of pre-existing co-crystals) is only 0.04M. Therefore, diffusion in the grain boundaries

569 must involve a fluid boundary layer on the co-crystals (as observed experimentally) and a
570 stabilized nanoconfined $LiPF_6$ supersaturated Adpn solution.

CONCLUSIONS

While much research has been expended to optimize crystal structures and doping strategies in inorganic solid electrolytes, there has been much less work on soft-solid crystals. There are significant differences in the structures and mechanisms of ion conduction between these two classes of electrolytes. In contrast to inorganic conductors, the soft-solid crystals of $(Adpn)_2LiPF_6$ have an interstitial solvent mediated migration of Li^+ ions, which we demonstrate is a fluid surface layer on the co-crystals and possibly a supersaturated $LiPF_6$/Adpn solution between the co-crystals. The weak interactions between the "hard" Li^+ ions and "soft" –C≡N groups, and the fewer contacts (four for –C≡N vs five for –O- in glymes[6]) are responsible for the three order of magnitude increase in conductivity compared with the crystalline solvate $(EO)_6LiPF_6$ ($\sigma \sim 10^{-7}$ S/cm) prepared using low molar mass polyethylene oxide[5,10]. Further, in the case of inorganic lithium electrolytes, the grain boundary resistance is believed to be greater than the bulk conductivity, while in the case of soft-solid crystals the grain boundaries are fluid and thus have better conductivity than the bulk grains.

Similar to the recent developments in ceramic electrolytes, improvements in conductivity for soft co-crystals are expected if 2D or 3D channel systems with a shorter distance between Li sites are synthesized. Another future modification would be to engineer a cocrystal with an optimal solvent and anion that increases the number of vacancy or interstitial sites (e.g., by isovalent or aliovalent doping, or introduction of defects by chain ends (here by introducing a different dinitrile or a mononitrile) as in the case of glyme/LiX complexes[9]). Future efforts will explore the incorporation of these deliberate defecting strategies to improve conductivity in these electrolytes.

METHODS

General

Lithium metal, $LiPF_6$ salt, Adpn, and diethyl ether (Et_2O) were purchased from Sigma-Aldrich. Et_2O was distilled using sodium benzophenone ketyl as a water/oxygen scavenger. Single-crystal and powder X-ray diffraction data were obtained on a Bruker KAPPA Apex II DUO with sealed-tube Mo Kα and Cu Kα sources, a TRIUMPH monochromator for the molybdenum tube, and an Oxford Cryostream low temperature device. Thermal degradation analysis of $(Adpn)_2LiPF_6$ crystals was carried out on a Thermogravimetric Analysis (TGA) TA Instruments Hi-Res TGA 2950 at a ramp rate of 10 °C min^{-1} with a flow of ultra-pure N_2 gas. A Differential Scanning Calorimeter (DSC) TA Instruments 2920 was used to analyze the melt and crystallization temperatures of the $(Adpn)_2LiPF_6$, with the sample in hermetically sealed Tzero aluminum pans. Samples were scanned from -120 °C to 200 °C at a scan rate of 10 °C.min^{-1}, under ultra-pure N_2 purge. The second cycle of the adiponitrile matrix and $(Adpn)_2LiPF_6$ powder was reported out of the two measured cycles. Scanning electron microscope (SEM) data were acquired on a FEI Quanta 450FEG SEM) with energy-dispersive X-ray spectroscopy (EDS) capability (Oxford Aztec Energy Advanced EDS System). Raman spectra were recorded in the 100-3000 cm^{-1} region at room temperature using a Horiba LabRAM HR Evolution Raman spectrometer, with a resolution of 1.8 cm^{-1}, an excitation wavelength of 532 nm, 60 mW power, and a grating groove density of 600 gr/mm. Samples were measured with 8 acquisitions, and 2 to 8 seconds each, depending on peak intensity.

For the conductivity measurements, polycrystalline $(Adpn)_2LiPF_6$ powder incorporated in the glass fiber separator or prepared by pressing at 800 psi in a hydraulic crimper in an argon purged glove

box, was used. The conductivity measurements were performed in a homemade electrochemical cell placed in a N_2 purged, temperature-controlled gas chromatography (GC) oven. Temperature-dependent bulk impedance data was measured by AC electrochemical impedance spectroscopy (EIS) using a Gamry Interface 1000 potentiostat/galvanostat/ZRA in the frequency range 0.1−1MHz in a temperature range between 80 ^{0}C and -10 ^{0}C with increments of 10 ^{0}C. The cell was thermally equilibrated for 30 minutes at each temperature before the bulk impedance was measured during both the cooling and heating cycles.

Synthesis:

$LiPF_6$ (151 mg, 1.0 mmols) was dissolved in excess adiponitrile (Adpn) (4.5 ml, 4.0 mmol) by heating the mixture to 165 ^{0}C under an argon atmosphere until it dissolved. The $LiPF_6$ was not soluble in Adpn at RT. Upon cooling, crystalline material started to form at about 115 ^{0}C and was complete at room temperature (RT). A single crystal was removed from the precipitate for X-ray structure determination, and the remaining solid was rinsed five times with excess Et_2O and dried under vacuum for ~ 20 minutes to remove the residual amount of Adpn and Et_2O, after which the dry, co-crystal solid was isolated; no visible liquid adiponitrile/solvent, was apparent by inspection. Water is rigorously excluded from all samples as we use a glove box with argon atmosphere where water levels are < 9 ppm at worst. The sample was incorporated concomitantly during the synthesis into Whatman glass microfiber filters (GF), grade GF/A (Sigma-Aldrich) 0.26 mm thickness. The co-crystal in the glass fiber filter was used as the separator between the electrodes to control the size and the amount of the electrolyte in the electrochemical experiments.

For all other electrochemical measurements (Li^+ ion transference numbers, plating and stripping, cyclic voltammetry, linear sweep voltammetry, and full cell cycling) the $(Adpn)_2LiPF_6$ was

637 incorporated in the glass filters (during the synthesis). Before use, the lithium metal was polished
638 using Teflon blocks. For the plating and striping experiments at room temperature with the
639 $Li^0/(Adpn)_2LiPF_6/Li^0$ cell, current densities of 0.01mA/cm^2 for 1 to 120 cycles, 0.05mA/cm^2 for
640 121 to 180 cycles, and 0.1 mA/cm^2 for 181 to 240 cycles were used. Li^+ ion transference numbers
641 were obtained by the method of combined ac and dc measurements[66,67]. The cathode was prepared
642 from $LiFePO_4$/carbon black/PVDF binder (8/1/1 by weight) using N-methyl-2-pyrrolidone (NMP)
643 to form a slurry that was doctor-bladed onto battery-grade aluminum foil to form 1.9-2.2 mg/cm^2
644 electrodes. The electrodes were dried in a vacuum oven overnight at 120°C. The dried electrodes
645 were calendared with a Durston flat agile F130 mm rolling mill mechanical presser.

646 **MD simulations:**

647 Force field parameters for bonded and Lennard Jones (vdW) interactions for Adpn were taken
648 from the OPLS all-atom force field[68]. The partial charges on all atoms of Adpn were calculated
649 from the MP2//aug-cc-PVDZ optimized structure using the CHELPG method[69]. Since the Li^+ ion
650 is present in tetra coordination with Adpn, the partial charge on Li^+ was calculated using the
651 optimized structure in **Figure S21** with a long range and dispersion corrected ωB97xD functional
652 with 6-311++G(d,p)$_{optimization}$/aug-cc-PVDZ $_{charge\ calculation}$ basis set. This calculation suggested a
653 partial charge of 0.845 e unit on the Li^+ ions. The charge value on the Li^+ ion (0.845e) was used
654 as the scaling factor to rescale the partial charges on PF_6^- ions (obtained from MP2//aug-cc-PVDZ
655 calculations, separately). To compute theoretical Raman spectra for Adpn and $(Adpn)_2LiPF_6$,
656 vibrational frequencies were calculated using PBE/6-311++G(d,p) for the structures optimized
657 using the same functional/basis set. All the gas phase quantum chemistry calculations were carried
658 out using the GAUSSIAN 9.0 software package[70]. Detailed protocol for force-field development
659 is provided in the **Supporting Information**.

660 A supercell of 5x5x5 unit cells (20,000 atoms) of $(Adpn)_2LiPF_6$ was constructed in a cuboid with
661 the dimensions of 55.35 x 64.75 x 63.25 $Å^3$. This model was used for simulations under periodic
662 boundary conditions to represent the bulk phase, and hence, is designated as model *P*. However,
663 since the surface atoms have a large contribution towards the conduction and decomposition of
664 these co-crystalline electrolytes, a different model *V* was used to understand the structure,
665 dynamics and thermal behavior at the surface. Model *V* was constructed by placing a 5x5x5
666 supercell in a cube of 200 Å/side. GROMACS 5.0.7 software[71] was used for simulations and
667 analysis along with VMD 1.9.3 software[72] for visualization of trajectories. The supercell models
668 were energy minimized using standard protocols and algorithms implemented in the code. All the
669 simulations for model *P* were carried out using *NpT* ensemble conditions, while for model *V*,
670 canonical ensemble conditions were used. Details of temperature and pressure couplings and other
671 MD parameters can be found in another work on a similar co-crystalline electrolyte material[51].

672 **Plane-wave periodic DFT calculations:**

673 To examine the mechanism of conduction at the atomic level with precise energetics, PW-DFT
674 calculations were performed using the QUANTUM ESPRESSO 6.1 software package[73]. A
675 projector-augmented-wave-basis set (Kresse-Joubert)[74] was used with PBE pseudopotentials[75]
676 with a cut-off of 60 Ry and 360 Ry for kinetic energy and electron density, respectively. A unit
677 cell of $(Adpn)_2LiPF_6$ cocrystals (from single-crystal XRD data) was relaxed in a fixed volume box
678 and later in a variable cell manner to energy minimize the crystal structure. A threshold of 10^{-7} Ry
679 was used for electronic optimization and 10^{-3} Ry/Bohr for force minimization. **Table S3** shows a
680 comparison of unit cell parameters obtained from single-crystal XRD data and variable cell
681 relaxation DFT calculations. To investigate the path of Li^+ ion conduction in the cocrystal, 1x1x2,
682 3x1x1 and 2x1x2 supercells were created and optimized using the above discussed protocols. Due

to the large system size of these supercells, all the calculations were performed with a Γ-only 1x1x1 k-mesh. For every supercell, a pair of Li^+ ion-defected configurations was used as an initial and final image for Nudged Elastic Band (NEB) calculations to interpolate the minimum energy path (MEP). Several sets of images were used to obtain the MEP, with a threshold of 0.1 eV/Bohr used for every individual image. Further, the MEP was refined using the climbing image (CI)-NEB method[76] with a more precise threshold of 0.01 eV/Bohr for every image along the path.

ASSOCIATED CONTENT

Supporting Information.

Powder X-ray diffraction, data, TGA, SEM, DC polarization and cycling data, additional details of simulation and DFT, and crystallographic tables. Crystallographic data is also available from the CCDC under deposition number 1986269.

Acknowledgements

Support of this work by the National Science Foundation under award 2138432, by DST Nanomission SR/NM/TP-13/2016, SERB DST CRG/2018/001536 and IUSSTF/JC-031/2017 is gratefully acknowledged. We acknowledge National Supercomputing Mission (NSM) 'PARAM Brahma' at IISER Pune, which is implemented by C-DAC and supported by the Ministry of Electronics and Information Technology (MeitY) and Department of Science and Technology (DST), Government of India, Temple's EFRC cluster which is supported by the Center for Complex Materials, an Energy Frontier Research Center funded by the U.S. Department of Energy, Office of Science, Basic Energy Sciences, under Award#DESC0012575, and Temple University's HPC clusters, which were supported in part by the National Science Foundation through major research instrumentation grant number 1625061 and by the US Army Research Laboratory under contract number W911NF-16-2-018 for computational resources. P. P.

acknowledges foreign Fulbright Program from USDOS for a visiting research fellowship. For SEM work, we acknowledge the CoE-NIC facility at Temple University founded on DoD DURIP Award N0014-12-1-0777 from the Office of Naval Research.

Author contributions

Prabhat Prakash[a,b], Birane Fall[a], Jordan Aguirre[a], Parameswara Rao Chinnam[c], Sumanth Chereddy[a], Dmitriy Dikin[d], Arun Venkatnathan[b], Stephanie L. Wunder[a]*, Michael J. Zdilla[a]**

B. F. discovered and optimized the synthesis of the electrolyte, obtained electrochemical and physical data and assisted in interpretation, constructed and tested electrochemical cells. P. P. led computational efforts on MD simulations and DFT calculations, assisted with optimization of synthetic protocol and assisted with electrochemical data collection and interpretation. J. A. collected and interpreted Raman data. S. C. prepared cathode composite, assisted with cell assembly and with electrochemical data interpretation. P. R. C. designed electrochemical experimental testing, devised experimental strategy, and assisted with data interpretation. D. D. Obtained SEM, EDS data and assisted with interpretation. A. V. supervised computational efforts. S. L. W. supervised electrochemistry and characterization efforts. M. J. Z. supervised synthetic and X-ray characterization efforts.

Competing interests

The authors declare no competing interests.

REFERENCES:

1. Fergus, J. W. Ceramic and polymeric solid electrolytes for lithium-ion batteries. *J. Power Sources* **195**, 4554–4569 (2010).

2. Gao, Z. *et al.* Promises, Challenges, and Recent Progress of Inorganic Solid-State Electrolytes for All-Solid-State Lithium Batteries. *Adv. Mater.* **30**, 1–27 (2018).

3. Palacín, M. R. Recent advances in rechargeable battery materials: a chemist's perspective. *Chem. Soc. Rev.* **38**, 2565 (2009).

4. Lau, J. *et al.* Sulfide Solid Electrolytes for Lithium Battery Applications. *Adv. Energy Mater.* **8**, 1–24 (2018).

5. Gadjourova, Z., Marero, D. M., Andersen, K. H., Andreev, Y. G. & Bruce, P. G. Structures of the polymer electrolyte complexes PEO6 : LiXF6 (X = P, Sb), determined from neutron powder diffraction data. *Chem. Mater.* **13**, 1282–1285 (2001).

6. MacGlashan, G. S., Andreev, Y. G. & Bruce, P. G. Structure of the polymer electrolyte poly(ethylene oxide)(6): LiAsF6. *Nature* **398**, 792–794 (1999).

7. Gadjourova, Z., Andreev, Y. G., Tunstall, D. P. & Bruce, P. G. Ionic conductivity in crystalline polymer electrolytes. *Nature* **412**, 520–523 (2001).

8. Zhang, C. H., Ainsworth, D., Andreev, Y. G. & Bruce, P. G. Ionic conductivity in the solid glyme complexes [CH3O(CH2CH2O)(n)CH3]: LiAsF6 (n=3,4). *J. Am. Chem. Soc.* **129**, 8700–8701 (2007).

9. Staunton, E., Andreev, Y. G. & Bruce, P. G. Factors influencing the conductivity of crystalline polymer electrolytes. *Faraday Discuss.* **134**, 143–156 (2007).

10. Stoeva, Z., Martin-Litas, I., Staunton, E., Andreev, Y. G. & Bruce, P. G. Ionic conductivity in the crystalline polymer electrolytes PEO6 : LiXF6, X = P, As, Sb. *J. Am. Chem. Soc.* **125**, 4619–4626 (2003).

11. Pearson, R. G. Absolute electronegativity and hardness: application to inorganic chemistry.

Inorg. Chem. **27**, 734–740 (1988).

12. Tanaka, K. *et al.* High Li-Ion Conductivity in Li{N(SO 2 F) 2 }(NCCH 2 CH 2 CN) 2 Molecular Crystal. *Nano Lett.* **20**, 8200–8204 (2020).

13. Chinnam, P. R., Clymer, R. N., Jalil, A. A., Wunder, S. L. & Zdilla, M. J. Bulk-Phase Ion Conduction in Cocrystalline LiCl·*N*,*N*-Dimethylformamide: A New Paradigm for Solid Electrolytes Based upon the Pearson Hard–Soft Acid–Base Concept. *Chem. Mater.* **27**, 5479–5482 (2015).

14. Chinnam, P. R. *et al.* A Self-Binding, Melt-Castable, Crystalline Organic Electrolyte for Sodium Ion Conduction. *Angew. Chemie Int. Ed.* **55**, 15254–15257 (2016).

15. Fall, B. *et al.* Crystal structure and ionic conductivity of the soft solid crystal: isoquinoline$_3$•(LiCl)$_2$. *Ionics (Kiel).* **24**, 343–349 (2018).

16. Fall, B. *et al.* Experimental and Theoretical Investigation of the Ion Conduction Mechanism of Tris(adiponitrile)perchloratosodium, a Self-Binding, Melt-Castable Crystalline Sodium Electrolyte. *Chem. Mater.* **31**, 8850–8863 (2019).

17. Abouimrane, A., Ding, J. & Davidson, I. J. Liquid electrolyte based on lithium bis-fluorosulfonyl imide salt: Aluminum corrosion studies and lithium ion battery investigations. *J. Power Sources* **189**, 693–696 (2009).

18. Abouimrane, A., Whitfield, P. S., Niketic, S. & Davidson, I. J. Investigation of Li salt doped succinonitrile as potential solid electrolytes for lithium batteries. *J. Power Sources* **174**, 883–888 (2007).

19. Alarco, P.-J., Abu-Lebdeh, Y., Abouimrane, A. & Armand, M. The plastic-crystalline phase of succinonitrile as a universal matrix for solid-state ionic conductors. *Nat. Mater.* **3**, 476–

481 (2004).

20. Choe, H. S., Carroll, B. G., Pasquariello, D. M. & Abraham, K. M. Characterization of Some Polyacrylonitrile-Based Electrolytes. *Chem. Mater.* **9**, 369–379 (1997).

21. Carol, P., Ramakrishnan, P., John, B. & Cheruvally, G. Preparation and characterization of electrospun poly(acrylonitrile) fibrous membrane based gel polymer electrolytes for lithium-ion batteries. *J. Power Sources* **196**, 10156–10162 (2011).

22. Zhou, D. *et al.* In Situ Synthesis of a Hierarchical All-Solid-State Electrolyte Based on Nitrile Materials for High-Performance Lithium-Ion Batteries. *Adv. Energy Mater.* **5**, 1500353 (2015).

23. Abraham, K. M. Li+-Conductive Solid Polymer Electrolytes with Liquid-Like Conductivity. *J. Electrochem. Soc.* **137**, 1657 (1990).

24. Watanabe, M., Kanba, M., Nagaoka, K. & Shinohara, I. Ionic conductivity of hybrid films composed of polyacrylonitrile, ethylene carbonate, and LiClO4. *J. Polym. Sci. Polym. Phys. Ed.* **21**, 939–948 (1983).

25. Croce, F., Brown, S. D., Greenbaum, S. G., Slane, S. M. & Salomon, M. Lithium-7 NMR and ionic conductivity studies of gel electrolytes based on polyacrylonitrile. *Chem. Mater.* **5**, 1268–1272 (1993).

26. Watanabe, M., Kanba, M., Nagaoka, K. & Shinohara, I. Ionic conductivity of hybrid films based on polyacrylonitrile and their battery application. *J. Appl. Polym. Sci.* **27**, 4191–4198 (1982).

27. Hong, H., Liquan, C., Xuejie, H. & Rongjian, X. Studies on PAN-based lithium salt complex. *Electrochim. Acta* **37**, 1671–1673 (1992).

28. Peramunage, D. Polyacrylonitrile-Based Electrolytes with Ternary Solvent Mixtures as Plasticizers. *J. Electrochem. Soc.* **142**, 1789 (1995).

29. Huang, B. Lithium ion conduction in polymer electrolytes based on PAN. *Solid State Ionics* **85**, 79–84 (1996).

30. Forsyth, M., Sun, J. & Macfarlane, D. R. Novel polymer-in-salt electrolytes based on polyacrylonitrile (PAN)-lithium triflate salt mixtures. *Solid State Ionics* **112**, 161–163 (1998).

31. Yoon, H.-K., Chung, W.-S. & Jo, N.-J. Study on ionic transport mechanism and interactions between salt and polymer chain in PAN based solid polymer electrolytes containing LiCF3SO3. *Electrochim. Acta* **50**, 289–293 (2004).

32. Ferry, A., Edman, L., Forsyth, M., MacFarlane, D. R. & Sun, J. Connectivity, ionic interactions, and migration in a fast-ion-conducting polymer-in-salt electrolyte based on poly(acrylonitrile) and LiCF3SO3. *J. Appl. Phys.* **86**, 2346–2348 (1999).

33. Forsyth, M., Sun, J., Macfarlane, D. R. & Hill, A. J. Compositional dependence of free volume in PAN/LiCF3SO3 polymer-in-salt electrolytes and the effect on ionic conductivity. *J. Polym. Sci. Part B Polym. Phys.* **38**, 341–350 (2000).

34. Hu, P. *et al.* Progress in nitrile-based polymer electrolytes for high performance lithium batteries. *J. Mater. Chem. A* **4**, 10070–10083 (2016).

35. Abu-Lebdeh, Y. & Davidson, I. New electrolytes based on glutaronitrile for high energy/power Li-ion batteries. *J. Power Sources* **189**, 576–579 (2009).

36. Xu, K. Electrolytes and Interphases in Li-Ion Batteries and Beyond. *Chem. Rev.* **114**, 11503–11618 (2014).

37. Li, W., Song, B. & Manthiram, A. High-voltage positive electrode materials for lithium-ion batteries. *Chem. Soc. Rev.* **46**, 3006–3059 (2017).

38. Nanini-Maury, E. *et al.* Electrochemical behavior of sebaconitrile as a cosolvent in the formulation of electrolytes at high potentials for lithium-ion batteries. *Electrochim. Acta* **115**, 223–233 (2014).

39. Tan, S., Ji, Y. J., Zhang, Z. R. & Yang, Y. Recent Progress in Research on High-Voltage Electrolytes for Lithium-Ion Batteries. *ChemPhysChem* **15**, 1956–1969 (2014).

40. Wang, X. *et al.* Adiponitrile as Lithium-Ion Battery Electrolyte Additive: A Positive and Peculiar Effect on High-Voltage Systems. *ACS Appl. Energy Mater.* **1**, 5347–5354 (2018).

41. Lee, S. H., Hwang, J., Park, S., Park, G. & Sun, Y. Adiponitrile (C 6 H 8 N 2): A New Bi-Functional Additive for High-Performance Li-Metal Batteries. *Adv. Funct. Mater.* **29**, 1902496 (2019).

42. Di Censo, D., Exnar, I. & Graetzel, M. Non-corrosive electrolyte compositions containing perfluoroalkylsulfonyl imides for high power Li-ion batteries. *Electrochem. commun.* **7**, 1000–1006 (2005).

43. Abu-Lebdeh, Y. & Davidson, I. High-Voltage Electrolytes Based on Adiponitrile for Li-Ion Batteries. *J. Electrochem. Soc.* **156**, A60 (2009).

44. Yamada, Y. *et al.* Unusual Stability of Acetonitrile-Based Superconcentrated Electrolytes for Fast-Charging Lithium-Ion Batteries. *J. Am. Chem. Soc.* **136**, 5039–5046 (2014).

45. Ugata, Y. *et al.* Li-ion hopping conduction in highly concentrated lithium bis(fluorosulfonyl)amide/dinitrile liquid electrolytes. *Phys. Chem. Chem. Phys.* **21**, 9759–9768 (2019).

46. Kerner, M., Plylahan, N., Scheers, J. & Johansson, P. Thermal stability and decomposition of lithium bis(fluorosulfonyl)imide (LiFSI) salts. *RSC Adv.* **6**, 23327–23334 (2016).

47. Farhat, D., Ghamouss, F., Maibach, J., Edström, K. & Lemordant, D. Adiponitrile-Lithium Bis(trimethylsulfonyl)imide Solutions as Alkyl Carbonate-free Electrolytes for Li 4 Ti 5 O 12 (LTO)/LiNi 1/3 Co 1/3 Mn 1/3 O 2 (NMC) Li-Ion Batteries. *ChemPhysChem* **18**, 1333–1344 (2017).

48. Oldiges, K., von Aspern, N., Cekic-Laskovic, I., Winter, M. & Brunklaus, G. Impact of Trifluoromethylation of Adiponitrile on Aluminum Dissolution Behavior in Dinitrile-Based Electrolytes. *J. Electrochem. Soc.* **165**, A3773–A3781 (2018).

49. Scheers, J. *et al.* Ion–ion and ion–solvent interactions in lithium imidazolide electrolytes studied by Raman spectroscopy and DFT models. *Phys. Chem. Chem. Phys.* **13**, 11136 (2011).

50. Murata, K., Asakawa, H., Nagashima, K., Furukawa, Y. & Sazaki, G. Thermodynamic origin of surface melting on ice crystals. *Proc. Natl. Acad. Sci.* **113**, E6741–E6748 (2016).

51. Prakash, P. *et al.* Unravelling the structural and dynamical complexity of the equilibrium liquid grain-binding layer in highly conductive organic crystalline electrolytes. *J. Mater. Chem. A* **6**, 4394–4404 (2018).

52. Wohde, F., Balabajew, M. & Roling, B. Li + Transference Numbers in Liquid Electrolytes Obtained by Very-Low-Frequency Impedance Spectroscopy at Variable Electrode Distances. *J. Electrochem. Soc.* **163**, A714–A721 (2016).

53. Ue, M., Takeda, M., Takehara, M. & Mori, S. Electrochemical Properties of Quaternary Ammonium Salts for Electrochemical Capacitors. *J. Electrochem. Soc.* **144**, 2684–2688

(1997).

54. Cheng, X.-B. & Zhang, Q. Dendrite-free lithium metal anodes: stable solid electrolyte interphases for high-efficiency batteries. *J. Mater. Chem. A* **3**, 7207–7209 (2015).

55. Ue, M., Ida, K. & Mori, S. Electrochemical Properties of Organic Liquid Electrolytes Based on Quaternary Onium Salts for Electrical Double-Layer Capacitors. *J. Electrochem. Soc.* **141**, 2989–2996 (1994).

56. Goodenough, J. B. & Kim, Y. Challenges for Rechargeable Li Batteries †. *Chem. Mater.* **22**, 587–603 (2010).

57. Yamada, Y. & Yamada, A. Superconcentrated Electrolytes to Create New Interfacial Chemistry in Non-aqueous and Aqueous Rechargeable Batteries. *Chem. Lett.* **46**, 1056–1064 (2017).

58. Qiu, Y., Lu, D., Gai, Y. & Cai, Y. Adiponitrile (ADN): A Stabilizer for the LiNi 0.8 Co 0.1 Mn 0.1 O 2 (NCM811) Electrode/Electrolyte Interface of a Graphite/NCM811 Li-Ion Cell. *ACS Appl. Mater. Interfaces* **14**, 11398–11407 (2022).

59. Zhang, J. *et al.* Regulating lithium deposition via electropolymerization of acrylonitrile in rechargeable lithium metal batteries. *Nano Energy* **88**, 106298 (2021).

60. Kerner, M. *et al.* Towards more thermally stable Li-ion battery electrolytes with salts and solvents sharing nitrile functionality. *J. Power Sources* **332**, 204–212 (2016).

61. Fong, R., von Sacken, U. & Dahn, J. R. Studies of Lithium Intercalation into Carbons Using Nonaqueous Electrochemical Cells. *J. Electrochem. Soc.* **137**, 2009–2013 (1990).

62. Gmitter, A. J., Plitz, I. & Amatucci, G. G. High Concentration Dinitrile, 3-Alkoxypropionitrile, and Linear Carbonate Electrolytes Enabled by Vinylene and

Monofluoroethylene Carbonate Additives. *J. Electrochem. Soc.* **159**, A370–A379 (2012).

63. Long, L. Z., Wang, S. J., Xiao, M. & Meng, Y. Z. Polymer electrolytes for lithium polymer batteries. *J. Mater. Chem. A* **4**, 10038–10069 (2016).

64. Xu, K. Nonaqueous liquid electrolytes for lithium-based rechargeable batteries. *Chem. Rev.* **104**, 4303–4417 (2004).

65. Van Hove, L. Correlations in space and time and born approximation scattering in systems of interacting particles. *Phys. Rev.* **95**, 249–262 (1954).

66. Bruce, P. G. & Vincent, C. A. Steady state current flow in solid binary electrolyte cells. *J. Electroanal. Chem.* **225**, 1–17 (1987).

67. Evans, J., Vincent, C. A. & Bruce, P. G. Electrochemical measurement of transference numbers in polymer electrolytes. *Polymer (Guildf).* **28**, 2324–2328 (1987).

68. Jorgensen, W. L., Maxwell, D. S. & Tirado-Rives, J. Development and testing of the OPLS all-atom force field on conformational energetics and properties of organic liquids. *J. Am. Chem. Soc.* **118**, 11225–11236 (1996).

69. Breneman, C. M. & Wiberg, K. B. Determining atom centered monopoles from molecular electrostatic potentials. The need for high sampling density in formamide conformational analysis. *J. Comput. Chem.* **11**, 361–373 (1990).

70. Frisch, M. J. *et al.* Gaussian 09, Revision E.01. (2009).

71. Abraham, M. J. *et al.* Gromacs: High performance molecular simulations through multi-level parallelism from laptops to supercomputers. *SoftwareX* **1**–**2**, 19–25 (2015).

72. Humphrey, W., Dalke, A. & Schulten, K. VMD: Visual molecular dynamics. *J. Mol. Graph.* **14**, 33–38 (1996).

73. Giannozzi, P. *et al.* Advanced capabilities for materials modelling with Quantum ESPRESSO. *J. Phys. Condens. Matter* **29**, 465901 (2017).

74. Kresse, G. & Joubert, D. From ultrasoft pseudopotentials to the projector augmented-wave method. *Phys. Rev. B* **59**, 1758–1775 (1999).

75. Perdew, J. P., Ernzerhof, M. & Burke, K. Rationale for mixing exact exchange with density functional approximations. *J. Chem. Phys.* **105**, 9982–9985 (1996).

76. Henkelman, G., Uberuaga, B. P. & Jónsson, H. A climbing image nudged elastic band method for finding saddle points and minimum energy paths. *J. Chem. Phys.* **113**, 9901–9904 (2000).